REPORT DOCUMENTATION PAGE

Form Approved
OMB No. 0704-0188

1. REPORT DATE *(DD-MM-YYYY)*
16/08/2016

2. REPORT TYPE
Final Report

3. DATES COVERED *(From - To)*
6/15/2012 – 9/15/2015

4. TITLE AND SUBTITLE
"Sea Spray Generation at a Rocky Shoreline"

5a. CONTRACT NUMBER
N00014-12-C-0290

5b. GRANT NUMBER

5c. PROGRAM ELEMENT NUMBER

6. AUTHOR(S)
Edgar L Andreas

5d. PROJECT NUMBER

5e. TASK NUMBER

5f. WORK UNIT NUMBER

7. PERFORMING ORGANIZATION NAME(S) AND ADDRESS(ES)

NorthWest Research Associates
PO Box 3027
Bellevue, WA 98009-3027

8. PERFORMING ORGANIZATION REPORT NUMBER
R135 – ONR S068P

9. SPONSORING / MONITORING AGENCY NAME(S) AND ADDRESS(ES)
Office of Naval Research
Attn: Dr. Scott Harper, ONR 322
875 North Randolph St
Arlington, VA 22203-1995

10. SPONSOR/MONITOR'S ACRONYM(S)

11. SPONSOR/MONITOR'S REPORT NUMBER(S)

12. DISTRIBUTION / AVAILABILITY STATEMENT

Distribution Statement A. Approved for public release; distribution is unlimited.

13. SUPPLEMENTARY NOTES

14. ABSTRACT

This Abstract is written by Dr. Joan Oltman-Shay, President of NWRA, on behalf of Dr. Ed Andreas, the PI on this project. Dr. Andreas worked on this project until his untimely death in late September 2015. A month earlier, he had just completed and submitted to the American Meteorology Society journal a paper representing and acknowledging work on this project. The paper, "Sea Spray Generation at Rocky Shoreline" by Ed Andreas was accepted for publication and as of July 2016 was being processed for publication.

15. SUBJECT TERMS
Need a few terms here

16. SECURITY CLASSIFICATION OF:			17. LIMITATION OF ABSTRACT	18. NUMBER OF PAGES	19a. NAME OF RESPONSIBLE PERSON
a. REPORT Unclassified	**b. ABSTRACT** Unclassified	**c. THIS PAGE** Unclassified	U	49	**19b. TELEPHONE NUMBER** *(include area code)* 425-556-9055

Sea Spray Generation at a Rocky Shoreline

Edgar L Andreas

NorthWest Research Associates, Inc.
Lebanon, New Hampshire

Corresponding author address: Dr. Edgar L Andreas, NorthWest Research Associates, Inc., 25 Eagle Ridge, Lebanon, NH 03766-1900.
E-mail: eandreas@nwra.com

July 2015

ABSTRACT

With sea ice in the Arctic continuing to shrink, the Arctic Ocean and the surrounding marginal seas will become more like the ocean at lower latitudes. In particular, with more open water, air-sea exchange will be more intense, and storms will be stronger and more frequent. The longer fetches over open water and the more energetic storms will combine to produce higher waves and more sea spray. Offshore structures—such as oil drilling, exploration, and production platforms—will face increased hazards from freezing sea spray.

Based on sea spray observations made with a cloud imaging probe at Mt. Desert Rock, an island off the coast of Maine, I quantify the spray that artificial islands built in the Arctic might experience. Mt. Desert Rock is small, low, unvegetated, and has an abrupt, rocky shoreline like these artificial islands. Many of the observations were at air temperatures below freezing. This paper reports the near-surface spray concentration and the rate of spray production at this rocky shoreline for spray droplets with radii from 6.25 to 143.75 μm and for wind speeds from 5 to 17 m s^{-1}. Spray concentration increases as the cube of the wind speed, but the shape of the concentration spectrum with respect to radius does not change with wind speed. Both near-surface spray concentration and the spray production rate are three orders of magnitude higher at this rocky shoreline than over the open ocean because of the high energy and resulting continuous white water in the surf zone.

1. Introduction

With the Arctic sea ice retreating farther and farther each summer, the Arctic Ocean is beginning to take on characteristics of the ocean at lower latitudes. In particular, heat lost from the now-open ocean can lead to more intense mesoscale storms; and the combination of storm winds and longer open water fetches will produce higher waves (e.g., Perrie et al. 2012; Asplin et al. 2012). Such evolving conditions will present new hazards for artificial structures like semi-submersible drilling rigs and man-made islands used as oil exploration and production platforms (Jones and Andreas 2009). Although the wind and waves themselves will create hazards for these structures, my interest here is the attendant sea spray produced.

Jones and Andreas (2009, 2012) previously considered the spray icing of semi-submersible drilling platforms that had fairly open profiles at the waterline such that most of the spray resulted from breaking waves in open water (also Minsk 1984a; Nauman 1984). Here, I turn to spray effects that small, artificial islands built in the Arctic Ocean can face: spray largely created by waves breaking along their shoreline. At sub-freezing temperatures, such spray will accumulate as ice on virtually all surfaces on these small islands (e.g., Minsk 1984b; Itagaki 1984). Even in above-freezing temperatures, the sea salt generated by high wind and waves will collect on raised structures and speed the corrosion of metal surfaces.

To quantify the rate of such shore-induced spray production, I carried out a month-long experiment in January 2013 on Mt. Desert Rock, an unvegetated island with low relief 24 miles out to sea from Bar Harbor, Maine. Mt. Desert Rock has a size and a topographic profile that is similar to some of the artificial islands now in the Arctic (e.g., Muzik and Kirby 1992; Gerwick 2007, Chapter 23). I presume that the spray concentrations and generation rates observed on Mt. Desert Rock will be similar to the values near other rocky shorelines and, in particular, will be what artificial islands in the Arctic might experience in the coming decades.

Although the literature contains several papers that report sea spray observations at shorelines, my data are unique in several ways. Climatologically, Mt. Desert Rock in January provides a good chance of encountering sub-freezing air temperatures and winds high enough to produce copious spray. And, indeed, roughly half of my measurements were made at temperatures below freezing. I am unaware of other spray data collected at temperatures below freezing.

Secondly, most of the previous spray measurements from the coastal zone looked at only relatively small droplets. For example, de Leeuw et al. (2000), Vignati et al. (2001), Clarke et al. (2006), van Eijk et al. (2011), and Piazzola et al. (2015) all reported recent spray observations in coastal regions, and all sampled droplets with radii at formation as small as 0.02 to 0.1 μm. Only van Eijk et al., however, sampled droplets with radii up to about 30 μm; the other papers reported on droplets with radii up to only 10–20 μm. While these small droplets are plentiful, they do not carry enough mass to produce the severe icing that larger droplets do (Jones and Andreas 2012).

Therefore, on Mt. Desert Rock, I collected spray data with a cloud imaging probe for which the smallest radius bin was centered at 6.25 μm and the instrument was capable of counting droplets with radii up to 775 μm. Although the counting statistics were poor for the largest droplets, I do report here spray concentration measurements for droplets in a radius bin centered at 143.75 μm—well into what is referred to as the *spume* regime for open ocean spray. Thus, I believe these observations represent the largest spray droplets that have been measured near a shoreline.

In this paper, I report data from the cloud imaging probe deployed for 27 days near the shoreline on Mt. Desert Rock. These data span 12.5-µm-wide radius bins with centers ranging from 6.25 to 143.75 µm and include 10-m winds from 5 to 17 m s^{-1}. A key finding is that the droplet spectra have the same shape at all observed wind speeds. I am thus able to derive an expression for the near-surface droplet concentration as the product of a function of just droplet radius and another function that goes as the cube of the wind speed. This concentration function, lastly, yields a function for predicting spray generation when ocean waves encroach on a rocky (as opposed to a sloping, sandy) shoreline.

2. Measurements on Mt. Desert Rock

Mt. Desert Rock, 24 miles into the Atlantic east of Bar Harbor, Maine, has a lightkeeper's house and a stone lighthouse that NOAA has instrumented as a C-MAN station under the National Data Buoy Center (NDBC). The College of the Atlantic in Bar Harbor owns Mt. Desert Rock and, as such, facilitates access to the "Rock" and provided us logistics support.

Figure 1 shows how small Mt. Desert Rock is and identifies the permanent structures there and the 2013 instrument locations. The "Rock" is truly a desert island: Its surface has no vegetation but is simply a rocky outcrop. From our survey (these numbers may differ from the NDBC information), the high point of the island is only 9.2 m above mean sea level; the lighthouse is 18 m tall. Prevailing winds at Mt. Desert Rock in January are westerly and northwesterly. We placed all instruments for best exposure to these winds.

To provide a rigid base and some security for the expensive cloud imaging probe (CIP; from Droplet Measurement Technologies), we mounted it on the foghorn platform (Fig. 1). As such, the probe was 3.24 m above local ground and 8.66 m above mean sea level. Because the wind speed and direction through the probe's laser array are crucial for computing spray concentration, the cloud imaging probe was rigidly attached to a Gill WindMaster sonic anemometer/thermometer (Fig. 2). The sonic's sample area was 0.48 m above the CIP's laser array. We frequently rotated this whole system to orient the cloud imaging probe into the wind. The appendix summarizes the equations that I used for obtaining spray concentration from the CIP.

To document near-surface meteorological conditions during our measurements, we deployed a "turbulence tripod" near the high-water line (Fig. 1). This tripod held a three-axis sonic anemometer/thermometer from Applied Technologies, Inc. (ATI), 2.35 m above ground, a

Li-Cor water vapor and carbon dioxide sensor 2.10 m above ground, and an Ophir hygrometer (which also measured air temperature) 2.23 m above ground. The ground here was 4.4 m above mean sea level.

I supplemented our own measurements with the NOAA measurements from the Mt. Desert Rock lighthouse; from another NOAA C-MAN station on nearby Matinicus Rock; and from two nearby buoys, 44034 and 44037, owned and maintained by the Northeastern Regional Association of Coastal Ocean Observing Systems.

Figures 3 and 4 show time series of meteorological and oceanographic data for January 2013 from these various sources. The winds denoted "MDR NOAA" and "Matinicus" were measured by the C-MAN instruments high on the Mt. Desert Rock and Matinicus lighthouses, respectively, and thus show higher speeds than the measurements nearer the surface from the two buoys and from the ATI and Gill sonics. These latter data are more representative of the wave and spray conditions and show that we sampled in winds up to about 17 m s^{-1}. The temperature panel in Fig. 3 shows that air temperatures were always less than 10°C during the measurements and were frequently below freezing. The stratification was generally unstable (water warmer than air; Figs. 3 and 4).

3. Data analysis

The appendix reviews the equations I used for processing measurements from the cloud imaging probe. Briefly, I computed spray concentrations in 12 radius bins, each 12.5-μm wide, from zero to 150 μm. The center radius in each bin locates the bin average in the upcoming plots and calculations.

The cloud imaging probe ran continuously, except when we stopped recording to reorient it into the wind. As such, from its 1 Hz measurements, I computed half-hour averages of spray concentrations for the first 30 minutes of an hour and for the second 30 minutes. For instances when the recording did not start at the top of the hour or end exactly at the top of the hour, I still computed averages from these partial 30-minute runs. I did, however, later exclude runs that were shorter than 15 minutes.

For the CIP site on Mt. Desert Rock, the counting statistics for the largest bins that the cloud imaging probe could sample were poor. Hence, the bin centered at a radius of 143.75 μm was the largest one that I retained for analysis. Moreover, for any bin, I retained its average only if it had counted at least ten droplets during the averaging period.

The Gill sonic anemometer attached to the cloud imaging probe sampled the three wind components and the sonic temperature roughly six times per second. I averaged these data over the same averaging periods as for the CIP. From the average along-wind ($\overline{U}$) and cross-wind ($\overline{V}$) components, I could compute the wind's average attack angle into the laser array of the cloud imaging probe. If this attack angle is not small, droplets hitting the thin arms that extend from the body of the CIP and hold the laser array (Fig. 2) can shatter; and the resulting smaller droplets can pass through the array and be counted. To minimize these erroneous counts, I kept for analysis only runs for which the attack angle of the wind was between –20° and +20°.

From $\overline{U}$, $\overline{V}$, and a measurement of the CIP's angular orientation, I also calculated the wind direction at the CIP in a true-north coordinate system. Figure 1 shows that for wind directions between 260° and 7° the CIP had best exposure to the ocean. My analysis includes only runs for which the average wind direction at the CIP was in this sector.

I also sequenced the analysis with the nearest tidal record, from Bar Harbor (NDBC station 8413220), and thereby assigned each half-hour run a tidal height. The arcs at 50 and 75 m in Fig. 1 show that, at high tide, the cloud imaging probe was well within 50 m of open water. Even at low tide, it was no more than about 75 m from open water and was often much closer.

Nevertheless, to judge whether distance from the water affected the spray counts, subsequent plots distinguish between the data collected during high water and low water. The tidal range during our observations was –0.43 to 3.93 m. Therefore, I designate as *low water* runs those collected when the tide was between –0.43 and 1.75 m; *high water* runs were collected when the tide was between 1.75 m and 3.93 m.

For measurements over the ocean, the neutral-stability wind speed at 10 m, U_{N10}, is commonly the independent variable in analyses and plots. I obtained U_{N10} from the Gill sonic. Its measurements of the three wind components yielded U_z, the average wind speed at height z_s for each half-hour CIP run. Similarity theory (e.g., Panofsky and Dutton 1984, p. 134) then relates U_z to the wind speed at 10 m:

$$U_{10} = U_z + \frac{u_*}{k}\left[\ln\left(\frac{10}{z_s}\right) - \psi_m\left(\frac{10}{L}\right) + \psi_m\left(\frac{z_s}{L}\right)\right]. \qquad (3.1)$$

Here, u_* is the friction velocity; k (= 0.40) is the von Kármán constant; z_s (= 3.72 m) is the height of the Gill sonic above the local surface; and ψ_m is a stratification correction that is a function of the Obukhov length, L.

Because, in subsequent analyses I ignore runs for which the 10-m wind speed was less than 5 m s^{-1} (because there was negligible spray) and because z_s and 10 m are relatively small, I ignore the stratification corrections in (3.1) because they are small. Hence, (3.1) yields a simpler expression for U_{N10}:

$$U_{N10} = U_z + \frac{u_*}{k}\ln\left(\frac{10}{z_s}\right). \tag{3.2}$$

Meanwhile, Andreas et al. (2012) deduced a relationship between u_* and U_{N10} from several thousand observations over the open ocean:

$$u_* = 0.239 + 0.0433\left\{\left(U_{N10} - 8.271\right) + \left[0.120\left(U_{N10} - 8.271\right)^2 + 0.181\right]^{1/2}\right\}. \tag{3.3}$$

Here, both u_* and U_{N10} are in m s^{-1}. Substituting (3.3) for u_* in (3.2) yields a single equation that relates the measurement, U_z, to the desired quantity, U_{N10}. I solved it using Newton's method and thereby obtained values for both U_{N10} and u_* for each CIP run.

To standardize the spray concentrations to a common height that will also be relevant for estimating the spray generation function, I extrapolated the spray observations to the height of the wave crests. I designate these concentrations C_0 and interpret them as the concentration at the sea surface (e.g., Fairall et al. 2009; Andreas et al. 2010). Fairall et al. (2009) used the following relation to convert the spray concentration at height z_1 to the concentration at height z_2:

$$C\left(z_2, r_0\right) = C\left(z_1, r_0\right)\left(\frac{z_2}{z_1}\right)^{-V_g(r_0)/k\,u_*\,f_s}. \tag{3.4}$$

Here, both concentrations are for droplets with a radius at formation of r_0, $V_g(r_0)$ is the terminal fall speed of these droplets, and f_s is related to the turbulent diffusivity of the droplets.

Because I want to estimate C_0, z_2 becomes $H_{1/3}/2$ (= $A_{1/3}$), the significant wave amplitude, where $H_{1/3}$ is the significant wave height (Fig. 4). In other words, z_2 is the average height above mean sea level of the wave crests. Fairall et al. (2009), among others, assume that $C(z_2,r_0)$ is constant between $A_{1/3}$ and the mean water surface. Consequently, $C(A_{1/3},r_0)$ is a reasonable estimate for C_0. As such, (3.4) becomes

$$C_0\left(r_0\right) = C\left(z_{CIP}, r_0\right)\left(\frac{A_{1/3}}{z_{CIP}}\right)^{-V_g(r_0)/k u_* f_s}, \tag{3.5}$$

where z_{CIP} is the height of the cloud imaging probe above the local surface.

For f_s in (3.5), I use (Rouault et al. 1991; Kepert et al. 1999; Fairall et al. 2009)

$$f_s\left(r_0, u_*\right) = \frac{1}{1 + 2\left[V_g\left(r_0\right)/\sigma_w\right]^2}, \tag{3.6}$$

where σ_w is the standard deviation of the vertical velocity fluctuations of the air. Continuing with the assumption of near-neutral-stratification, I use for σ_w in (3.6) 1.25 u_* (Kaimal and Finnigan 1994, p. 16).

Lastly, $A_{1/3}$ in (3.5) comes from the algorithm that Andreas and Wang (2007) derived from data collected by NDBC buoys off the northeast coast of the United States, including several in the vicinity of Mt. Desert Rock. Figure 4 compares the estimates of $H_{1/3}$ from this algorithm with the data from buoys 44034 and 44037. Agreement between the Andreas and Wang algorithm and the buoy data is generally good, but the Andreas and Wang algorithm does predict a non-zero lower limit for $H_{1/3}$ in light winds. This lower limit is obvious in Fig. 4 but is not an issue for this analysis because it occurs when the wind speed was less than 5 m s^{-1}, and I ignore these wind speeds in the upcoming results.

4. Sea spray concentration

Figures 5 and 6 show the near-surface spray droplet concentration spectra (i.e., C_0) as measured by the cloud imaging probe. Each panel breaks out measurements for wind speeds (U_{N10} in this case) in ranges between 6 and 17 m s^{-1}. Each panel also identifies measurements made during high water and low water.

Figures 5 and 6 do not reveal any obvious differences between the measurements made during high water and low water. Both the magnitude of the concentrations and the shape of the spectra as a function of radius are similar for the two types of observations.

In fact, in Figs. 5 and 6, the spectral shape seems to be the same for all wind speeds. I therefore nondimensionalized all the spectra in Figs. 5 and 6 with the concentration measured at $r_0 = 6.25$ μm for each spectrum. Figure 7 plots nondimensional versions of all 363 spectra collected in wind speeds of 5 m s^{-1} and higher. Still here, the figure distinguishes the 170 spectra collected during high water from the 163 spectra collected during low water to reiterate that the distance to open water does not seem to have influenced the results. That is, the medians for all the data in a radius bin and the medians for just the high water and low water observations in a bin are all largely indistinguishable.

The four small-radius bins in Fig. 7 fall on a straight line on this log-log plot,

$$\ln\left[C_0(r_0)/C_0(r_0\!=\!6.25\mu\mathrm{m})\right] = 3.39396 - 1.85201\ln(r_0); \tag{4.1}$$

the six large-radius bins similarly fall along another straight line,

$$\ln\left[C_0(r_0)/C_0(r_0\!=\!6.25\mu\mathrm{m})\right] = 21.71391 - 6.31974\ln(r_0). \tag{4.2}$$

I can therefore derive a hyperbola to fit the entire nondimensional spectrum,

$$\ln\left[C_0(r_0)/C_0(r_0{=}6.25\,\mu\text{m})\right] = -4.20022 \\ -4.08587\left\{\left[\ln(r_0) - 4.10051\right] + \left\{0.29891\left[\ln(r_0) - 4.10051\right]^2 + 0.78383a^2\right\}^{1/2}\right\} . \quad (4.3)$$

Here, a is a coefficient that moves the knee of the hyperbola as close to the intersection of lines (4.1) and (4.2) as I desire; $a = 0.10$ produces the best-fitting hyperbola. Figure 7 shows this result.

Conceptually, we can use (4.3) to predict spray concentration if we can associate a wind speed dependence for the spectra plotted in Figs. 5 and 6. All we need to know is how $C_0(r_0 = 6.25\ \mu\text{m})$, the concentration for droplets in the bin centered at 6.25 μm used to nondimensionalized the spectra in Fig. 7, depends on wind speed.

To evaluate this wind speed dependence, I first looked at the wind speed dependence of all the concentration data because any wind speed dependence that I assign to the 6.25-μm radius bin must be appropriate for all radius bins up to 143.75 μm. Figure 8 therefore plots normalized droplet concentrations from all 333 droplet spectra. I calculated these normalized concentrations by dividing all concentrations in a specific radius bin by the average concentration for that bin. Consequently, the normalized concentrations in Fig. 8 tend to distribute equally below and above one.

I fitted straight lines through the log-log data in Fig. 8. The standard approach is to do least-squares linear regression with y as the dependent variable and x as the independent variable. When both x and y have comparable uncertainties, however, such a fitting can be biased because least-squares algorithms presume that the x values are perfectly known. Consequently, I also like to derive a fitting relation from the bisector of y-versus-x and x-versus-y least-squares fits (e.g., Andreas 2002a). Figure 8 also shows this bisector fit. Lastly, since both fitting lines are close to cubic in wind speed, Fig. 8 shows the cubic relation for which the normalized concentration goes as U_{N10}^3.

In Fig. 8, the cubic relation splits the *y*-versus-*x* and bisector fits and, by eye, does best at representing the data for all radius bins and for all wind speeds. I thus represent the concentration data for the 6.25-μm radius bin with a cubic relation in U_{N10}. Figure 9 shows that representation, which is

$$C_0\left(r_0 = 6.25\,\mu\mathrm{m}\right) = 100.38\,U_{N10}^3 . \tag{4.4}$$

This gives $C_0(r_0 = 6.25\ \mu\mathrm{m})$ in m^{-3} μm^{-1} for U_{N10} in m s^{-1}.

I close the discussion of Fig. 8 by pointing out, again, that the data collected during high water do not differ appreciably from the data collected during low water.

Combining (4.4) and (4.3) produces an expression to fit the near-surface spray concentrations measured on Mt. Desert Rock:

$$\begin{aligned} C_0\left(r_0, U_{N10}\right) = {} & 100.38\,U_{N10}^3 \exp\Big[-4.20022 \\ & -4.08587\left\{\left[\ln\left(r_0\right) - 4.10051\right] + \left\{0.29891\left[\ln\left(r_0\right) - 4.10051\right]^2 + 0.0078383\right\}^{1/2}\right\}\Big] . \end{aligned} \tag{4.5}$$

Again, C_0 is in m^{-3} μm^{-1} when U_{N10} is in m s^{-1} and r_0 is in μm.

With the green curves, each panel in Figs. 5 and 6 displays (4.5), where U_{N10} for each green curve is taken as the mid-range wind speed for the wind speed range indicated in the panel. I draw two conclusions from these green curves. First, the shape of the droplet spectra is consistent for all the wind speeds depicted. Second, the cubic dependence on U_{N10} does well in representing the spectral levels at all wind speeds in the dataset.

5. Spray generation function

The spray generation function, which I henceforth denote as dF/dr_0 (e.g., Monahan et al. 1986; Andreas 2002b), predicts the number of spray droplets with initial radius r_0 that are produced per square meter of sea surface per second per micrometer increment in droplet radius. Its units are thus $\mathrm{m}^{-2}\ \mathrm{s}^{-1}\ \mu\mathrm{m}^{-1}$, where r_0 is expressed in micrometers.

Often, dF/dr_0 is calculated as the near-surface droplet concentration, $C_0(r_0)$, times some velocity scale (e.g., Moore and Mason 1954; Fairall and Larsen 1984; Smith et al. 1993; Lewis and Schwarz 2004, p. 101; Hoppel et al. 2005; de Leeuw et al. 2011). This approach makes the reasonable assumption that, to be observed, spray droplets need some upward velocity to be entrained in the air flow. Andreas et al. (2010) evaluated the usefulness of this approach for four distinct velocity scales—the dry deposition velocity, which can be close to the terminal fall velocity; a turbulent droplet diffusion velocity; the jet droplet ejection velocity; and the wind speed evaluated at the significant wave amplitude, $U_{A_{1/3}}$. For the droplets like those observed at Mt. Desert Rock—with radii of about 10 μm and larger—Andreas et al. concluded that $U_{A_{1/3}}$ is the best velocity scale for predicting spray generation from the near-surface concentration. Therefore, I estimate the spray generation function as

$$\frac{dF}{dr_0} = U_{A_{1/3}} C_0\left(r_0, U_{N10}\right), \tag{5.1}$$

where C_0 comes from (4.5).

Figure 10 shows this spray generation function for a range of wind speeds. Finding U_{N10} and $U_{A_{1/3}}$ values to use in (5.1) is crucial. To compute these, I first run the new bulk flux algorithm that Andreas et al. (2015) describe; from sea surface temperature (T_s) and from wind speed (U_r), air temperature (T_a), and relative humidity (RH_r) at arbitrary reference height r, it computes, among other quantities, the friction velocity u_* and the Obukhov length L. Equations like (3.1) and (3.2) yield $U_{A_{1/3}}$ and U_{N10} as

$$U_{A_{1/3}} = U_r + \frac{u_*}{k}\left[\ln\left(\frac{A_{1/3}}{r}\right) - \psi_m\left(\frac{A_{1/3}}{L}\right) + \psi_m\left(\frac{r}{L}\right)\right] \tag{5.2}$$

and

$$U_{N10} = U_r + \frac{u_*}{k}\ln\left(\frac{10}{r}\right). \tag{5.3}$$

For comparison with an open ocean spray generation function, I also plot in Fig. 10 the function that Andreas et al. (2010) created by smoothly joining the bubbles-only function from Monahan et al. (1986) with the large-radius function that Fairall et al. (1994) formulated from an earlier function from Andreas (1992). After reviewing the field, Andreas (2002b) had concluded that the Monahan et al. function provides an "anchor" for predicting the generation of small droplets over the open ocean while the Fairall et al. function has the best overall properties for high winds and larger droplets.

Furthermore, the merging is fairly easy: Both functions take as their wind speed dependence the whitecap coverage (W) that Monahan and O'Muircheartaigh (1980) deduced,

$$W\left(U_{10}\right) = 3.8\times10^{-6}\,U_{10}^{3.4}. \tag{5.4}$$

In this, W is the fractional whitecap coverage, and U_{10} is the wind speed at 10 m.

In Fig. 10, (5.1) is roughly three orders of magnitude larger than the joint Monahan and Fairall function for droplets smaller than about 30 μm in radius. As the radius increases, this difference decreases until the level of (5.1) extrapolated to r_0 = 200 μm is very close to the level of the joint Monahan and Fairall function. The large-radius slope of my new function is also very close to the large-radius slope of the Monahan and Fairall function.

Previously, de Leeuw et al. (2000) measured surf zone production at the Scripps pier in La Jolla, California. Likewise, van Eijk et al. (2011) measured surf zone production at La Jolla and also at the Field Research Facility in Duck, North Carolina. Both of these surf zones are characterized by gently sloping beaches in contrast to the abrupt, rocky shoreline and the absence of a beach at Mt. Desert Rock. de Leeuw et al. concluded that the breaking waves at the La Jolla site enhanced spray production by up to two orders of magnitude. For their two sites, van Eijk et al. concluded that the surface zone added 0.7 to one order of magnitude to the spray concentration. Remember, though, both groups observed spray droplets with radii no bigger than 30 μm.

The next section continues this discussion of the enhanced spray production that I observed.

6. Discussion

a. Footprint analysis

The explanation for the magnitude of the spray flux observed at Mt. Desert Rock is intimately tied to the upwind footprint that influenced measurements at the cloud imaging probe. Classically, the flux footprint is a function of distance (x) upwind from an instrument, which is at height z_m; the origin of this distance is at the instrument. By integrating over all x the surface flux at location x multiplied by the footprint function at x, we derive the flux at the origin and at height z_m that the instrument sees (e.g., Horst and Weil 1992, 1994; Wilson 2015).

Besides z_m, which is 3.24 m for the cloud imaging probe, another parameter that is important in most footprint analyses is the aerodynamic roughness length z_0. For a typical wind speed in my dataset, 12 m s^{-1}, I estimate $z_0 = 3.4\times10^{-4}$ m. Hence, z_m/z_0, another important quantity, is about 9500. The height of the atmospheric boundary layer, h, and the ratio z_m/h are also required in some footprint analyses. Without measurements of h, I surmise that it was rarely less than 400 m; therefore, $z_m/h \leq 0.008$.

The footprint function is zero for some distance immediately upwind of the instrument (Horst and Weil 1994; Hsieh et al. 2000; Wilson 2015). In essence, material escaping the surface too close to the instrument does not have time to reach height z_m and be observed before it is blown beyond the instrument. I denote this distance X for "excluded."

The total upwind extent of the flux footprint itself I denote as F (in meters). From figures in Kljun et al. (2004; e.g., Fig. 1), I estimate that, for the given values of z_m, z_0, h, and stratification, the footprint is approximately zero for F larger than about 200 m. In other words, the CIP is most sensitive to the surface within 200 m upwind from it. Meanwhile, the peak of the footprint function—the region of upwind fetch that contributes the most to observations at height z_m—is roughly 50–70 m upwind of the instrument (Horst and Weil 1994, Fig. 3; Kljun et al., Fig. 1). From Fig. 1, we can therefore conclude that most of the spray reaching the cloud imaging probe originated in or near the surf zone.

Let us suppose that this surf zone has a width S. But S is not constant; I observed it to increase with wind speed (and the resulting wave energy) such that it was about 30 m wide for the highest wind speeds we encountered on Mt. Desert Rock, about 20 m s^{-1}. As a crude estimate to model this wind speed effect on the surf zone, I use

$$S = 30\left(\frac{U_{N10}}{20}\right)^3, \tag{6.1}$$

where S is in meters when U_{N10} is in m s^{-1}. This choice of a cubic dependence on U_{N10} recognizes that the energy flux that the wind puts into the ocean—and which, in turn, builds the waves that create the surf zone—scales with the cube of the wind speed (e.g., Wu 1979).

With this conceptual framework, I can predict how the quantity of spray produced in a surf zone might differ from spray over the open ocean. Over the open ocean, the spray measured by a cloud imaging probe at height z_m would scale something like

$$\text{Ocean:} \quad W\left(U_{10}\right)\left(F - X\right). \tag{6.2}$$

The spray actually measured by the CIP at Mt. Desert Rock, on the other hand, would scale like

$$\text{MDR:} \quad W\left(U_{10}\right)\left(F - S - R\right) + 1\cdot\gamma\cdot S + 0\cdot R. \tag{6.3}$$

Both of these equations rest on the common practice of inferring spray production from whitecap coverage.

In (6.2) and (6.3), $W(U_{10})$ is the fractional whitecap coverage for the open ocean as estimated from (5.4). In (6.3), R is the distance over rock from the CIP to the shoreline on Mt. Desert Rock; I estimate it as, typically, 30 m (see Fig. 1). This portion of the footprint obviously produces no spray; the footprint function is thus zero here. In contrast, the surface zone is one continuously renewed whitecap; the fractional whitecap coverage is 1 here (de Leeuw et al. 2000; i.e., the 1 multiplying the S term in (6.3)). Moreover, as I will discuss shortly, the surf zone is more productive white water than would be characterized by just whitecap coverage, (5.4). Therefore, I include the γ coefficient in the S term and expect γ to be one or greater.

By taking the ratio of (6.3) to (6.2), we can estimate how productive the surf zone at Mt. Desert Rock is compared to the open ocean:

$$Ratio = \frac{W(U_{10})(F - S - R) + \gamma S}{W(U_{10})(F - X)}. \tag{6.4}$$

For demonstration purposes and because R and X are relatively small compared to F, I set $X = R$. Then (6.4) reduces to

$$Ratio = \frac{\gamma S}{W(U_{10})(F - R)} + 1 - \frac{S}{F - R}. \tag{6.5}$$

The white water in the surf zone more closely resembles a stage A whitecap than a stage B whitecap. Stage A whitecaps are associated with actively breaking waves, while stage B whitecaps result from the rising, decaying bubble plumes left after a wave breaks (Monahan and Lu 1990). The surf zone at Mt. Desert Rock during winds of 10 m s^{-1} and higher was a very energetic and turbulent region of total white water and continually breaking waves (cf. Brocchini and Peregrine 2002).

Woolf et al. (1987) and Cipriano et al. (1987) studied spray formation in a laboratory whitecap simulation tank. Although they could measure only spray droplets with radii of about 10 μm or less, their result are, nevertheless, suggestive of what we might see on Mt. Desert Rock. Figures 4 and 5 in Woolf et al. and Fig. 2 in Cipriano et al. suggest that a newly formed whitecap (the stage A whitecap) produces about an order of magnitude more spray droplets per unit time than the later decaying phase (stage B) of the whitecap. On reevaluating these papers, Ed Monahan (2015, personal communication) estimated that the production of these droplets, which have radii at the small end of my spectrum, may even be up to two orders of magnitude higher in stage A whitecaps than in stage B whitecaps.

These studies by Woolf et al. (1987) and Cipriano et al. (1987) generally quantified only the spray production by bursting bubbles—that is, film and jet droplets. In the surf zone, with an onshore wind, other mechanisms can also create spray droplets (e.g., Peregrine 1983; Monahan et al. 1986; Andreas et al. 1995, Fig. 1; Brocchini and Peregrine 2002). Spume droplets, which the wind tears right off the wave crests (e.g., Soloviev et al. 2012), are generally larger than film and jet droplets. In the very turbulent surf zone, where waves reflected from the steep shore collide with incoming waves from the ocean, so-called splash and chop droplets also occur. It is therefore not implausible to speculate that these latter processes, especially, can enhance the spray production another order of magnitude.

In summary, spray production in a surf zone at a rocky shoreline, where white water is ubiquitous and continually renewed, could be 10 to 1000 times higher at comparable winds speeds than over the open ocean, where spray production predominantly comes from stage A and stage B whitecaps. Therefore, Fig. 11 displays the ratio in (6.5) for γ ranging from 1 to 1000.

Although their geometry was somewhat different than for my observations on Mt. Desert Rock, the $\gamma = 1$ and $\gamma = 10$ cases in Fig. 11 approximate the data that de Leeuw et al. (2000) and van Eijk et al. (2011) obtained downwind of far less energetic surf zones over sloping beaches. Even if the breakers on their beaches were not more effective spray producers than open ocean whitecaps—that is, assuming $\gamma = 1$—Fig. 11 suggests that the spray production would still be enhanced by a factor of 3 or 4 because of the increased whitecap coverage.

Meanwhile, according to Fig. 11, a γ value between 100 and 1000—which according to my literature review seems to be possible—would explain the observed spray concentrations and spray generation function (Fig. 10), where the Mt. Desert Rock values are about three orders of magnitude larger than over the open ocean.

b. Parameterizing the spray

The debate on how to parameterize near-surface spray concentration and the spray generation function has gone back and forth for about 35 years. One approach assumes that the shape of the spray distribution with radius at formation r_0 is independent of forcing variables like wind speed, wave field, or water temperature. Then the near-surface spray concentration (as a function of just radius and wind speed for demonstration purposes) could be formulated as the product of a shape function, $f(r_0)$, and a forcing function, $g(U_{10})$:

$$C_0\left(r_0, U_{10}\right) = f\left(r_0\right) g\left(U_{10}\right). \tag{6.6}$$

de Leeuw et al. (2011) reviewed this concept; and it has found application in spray generation functions formulated by Monahan et al. (1986, their bubbles-only function), Fairall et al. (1994), and Andreas et al. (2010), among others.

The second school of thought supposes that the shape of the droplet spectrum depends on the forcing variables; and, therefore, separating the size function and the forcing function as in (6.6) is not possible. Monahan et al. (1983) seemed to document this change in the droplet spectrum with wind speed when they observed enhanced droplet counts for large droplets at higher wind speeds. Miller and Fairall (1988) put this approach in practice when they synthesized from four datasets a spray generation function for which the shape changed with wind speed. Andreas (1992), for example, was an early user of this Miller and Fairall function.

Smith et al. (1993) and later Smith and Harrison (1998) likewise derived spray generation functions for which the shape of the droplet spectrum changed with wind speed.

My observations, however, come down on the side of (6.6)—that the droplet spectrum does not change shape significantly with wind speed or other forcing variables for wind speeds between 5 and 17 m s^{-1}. In view of Figs. 5, 6, and 7, this conclusion is very robust.

Admittedly, the references cited in this section were all to open ocean conditions. Hence, it is not clear that the data from Mt. Desert Rock can be extended to the open ocean and, thereby, can add weight to either side of the argument on how to parameterize C_0 and dF/dr_0. I, nevertheless, felt it essential to interpret my data in the context of this debate.

c. Height profile of the spray

To assess icing and sea salt accumulation on structures downwind of a shoreline where spray is forming, we need to model the profile of the spray as a function of vertical coordinate z. Equations that have appeared earlier provide the solution. Namely, we can rearrange (3.5) to get the spray concentration profile:

$$C(z, r_0, U_{N10}) = C_0(r_0, U_{N10}) \left(\frac{z}{A_{1/3}} \right)^{-V_g(r_0)/k u_* f_s} . \qquad (6.7)$$

Furthermore, we can substitute (4.5) for $C_0(r_0, U_{N10})$. Equation (3.6) shows how to calculate f_s.

To continue with the calculation, readers can use their favorite algorithms for computing V_g and u_*. Alternatively, they can retrieve from http://people.nwra.com/resumes/andreas/software.php a bulk flux algorithm that Andreas et al. (2015) developed for computing u_* over the ocean, among other fluxes, and a second algorithm for fast microphysical calculations that include computing V_g (Andreas 2005).

7. Conclusions

With increasing wind speed, the surf zone at the rocky shore of Mt. Desert Rock became increasingly energetic. Active wave breaking, ubiquitous stage A whitecaps, and continuous turbulent white water grew oceanward from the shoreline with increasing winds. A cloud imaging probe placed a few tens of meters downwind from this surf zone counted the spray droplets generated there.

For 10-m, neutral-stability wind speeds (U_{N10}) between 5 and 17 m s^{-1}, I thus documented the near-surface concentration of spray droplets in 12 12.5-µm-wide bins with centers from 6.25 to 143.75 µm. One of the main results is that the shape of these near-surface concentration spectra, $C_0(r_0,U_{N10})$, as a function of droplet radius at formation, r_0, is independent of wind speed. I could, thus, formulate an expression for the near-surface concentration in terms of two independent functions:

$$C_0\left(r_0,U_{10}\right) = f\left(r_0\right) g\left(U_{10}\right), \tag{7.1}$$

where $f(r_0)$ is a shape function and $g(U_{N10})$ is a wind speed function. Equations (4.3) and (4.4), respectively, give these two functions.

Because of the high energy in the surf zone and the fact that a footprint analysis suggests that the cloud imaging probe focused preferentially on spray coming from the surf zone, the measured spray concentrations are two to three orders of magnitude higher than those measured over the open ocean. Waves crashing against rocks also produce one to two orders of magnitude more spray than waves breaking on sloping beaches.

The spray generation function derived from these near-surface concentration measurements reiterates how much more productive the surf zone is than is the open ocean. Figure 10 shows that, at least for droplets smaller than about 30 µm in r_0, the surf zone at Mt.

Desert Rock was three orders of magnitude more productive than the open ocean.

For droplets above 100 μm in radius, on the other hand, the Mt. Desert Rock spray generation function is comparable to the open ocean function. There are two possible explanations for this convergence for large radii. Either the joint Monahan et al. (1986) and Fairall et al. (1994) function overestimates the generation rate of the largest droplets or, at the CIP site on Mt. Desert Rock, many of the larger droplets settled out of the air flow before the CIP could count them. Both explanations are plausible because the counting statistics for the CIP were best for the smaller droplets, while the joint Monahan and Fairall function for open ocean spray generation shown in Fig. 10 is also most reliable for the smaller droplets. In summary, the orders-of-magnitude difference in spray concentration and in spray generation (Fig. 10) between Mt. Desert Rock and the open ocean is robust for droplet radii less than 50–100 μm.

Because these observations on Mt. Desert Rock are the first spray measurements at a rocky shoreline, I cannot say how general the results are. The footprint analysis in Section 6a provides justification for presuming that production in the surf zone at a rocky shoreline should be 2–3 orders of magnitude higher than over the open ocean. Moreover, its correct order-of-magnitude prediction for spray production over a sloping, sandy beach provides validation for that analysis. Consequently, although (4.5) and (5.1) may not be perfectly transferrable to other abrupt shores, they should be useful planning tools for evaluating how hazardous spray icing and sea salt might be for artificial islands currently built or planned for the high-latitude ocean.

Acknowledgments. I thank Kathy Jones of CRREL for help in the field, advice on the analysis, and comments on the manuscript. I also thank Captain Toby Stephenson of the *MV Osprey* for getting us and our equipment safely to and from Mt. Desert Rock; Chris Tremblay, Alex Borowicz, Tanya Lubansky, and Lindsey Nielsen for logistics support and company on the "Rock"; and Chris Fairall, Dan Wolfe, and Sergio Pezoa of NOAA/ESRL for loaning me their cloud imaging probe and instructing me in its use. Emily Moynihan of BlytheVisual created Fig. 1 from a similar image that Chris Tremblay provided. The U.S. Office of Naval Research supported me in this work with awards N00014-12-C-0290 and N00014-11-1-0073.

APPENDIX

Obtaining Droplet Concentration from the Cloud Imaging Probe

The cloud imaging probe (CIP; from Droplet Measurement Technologies, Inc., Boulder, Colorado) uses single-particle optical imaging with a linear array of 64 photodetectors to count and size droplets. The following equations that I used to process the raw CIP data come from the user's manuals (Anonymous 2009, 2012) and from software that Chris Fairall (2012, personal communication) shared with me.

The CIP uses a red laser; the wavelength is $\lambda = 0.660$ μm. The resolution in size bins is $R = 25$ μm: that is, the CIP counts droplets in size bins that increase from zero in steps of 25 μm in diameter. The CIP has a linear array of 64 (= ND) diode detectors; it thus can sort droplets into 62 (= NB) bins, each 25-μm wide.

I do the analysis, however, in terms of droplet radius; thus, the radius resolution is $\Delta r = R/2 = 12.5$ μm. With 62 CIP bins of width Δr, the upper radius limit for each bin (Bin_{Hi}) increases as $12.5i$, where $i = 1,62$. Hence, $Bin_{Hi} = 12.5, 25, 37.5, 50, \ldots, 762.5, 775$ μm. Likewise, the lower limit on each radius bin (Bin_{Lo}) goes as $12.5(i - 1)$, where $i = 1,62$. That is, $Bin_{Lo} = 0, 12.5, 25, 37.5, \ldots, 750, 762.5$ μm. My convention is to use the center radius of each bin to denote droplets counted by the CIP at a given radius. The center radius of a bin (in μm) is $Bin_{cent} = 6.25 + 12.5(i - 1)$, where $i = 1,62$.

On Mt. Desert Rock, the counting statistics for 30 minutes of sampling were poor for droplets beyond the bin centered at 143.75 μm. Hence, my plots show only droplets centered in the 12 bins 6.25, 18.75, 31.25, 43.75, …, 131.25, 143.75 μm.

Approximately every second, the CIP reported the number of droplets counted in each of its 62 bins. Call this one-second value the count K in bin i at time j, $K(j,i)$. The number of droplets counted in bin i in 30 minutes is simply the sum of all these counts:

$$\overline{K}(i) = \sum_{j=1}^{\sim 1800} K(j,i). \qquad \text{(A1)}$$

To find the droplet concentration in bin i for the 30 minutes, we must divide the bin sum by the total volume of air sampled (V) and by the bin width, Δr:

$$C(i) = \frac{\overline{K}}{V\,\Delta r}. \qquad \text{(A2)}$$

This has units of a droplet concentration: number of droplets per cubic meter of air per micrometer increment in droplet radius.

The volume V depends on the size bin. We first calculate the length of the diode array for droplets of size i:

$$L_{CIP}(i) = 2 \cdot 0.001 \cdot \Delta r \left(ND - i - 1\right), \qquad \text{(A3)}$$

where $i = 1,62$ and the 0.001 converts Δr in micrometers to millimeters. Thus, the lengths of the bins are $L_{CIP}(1) = 1.550$ mm, $L_{CIP}(2) = 1.525$ mm, $L_{CIP}(3) = 1.500$ mm, …, $L_{CIP}(61) = 0.050$ mm, $L_{CIP}(62) = 0.025$ mm.

The second length scale is the distance across the laser array, $zz(i)$. Again, this distance is a function of size bin but also of the laser optics. From Chris Fairall (2012, personal communication),

$$zz(i) = \min\left\{1580\, DOF0\left[0.001\, Bin_{Hi}(i)\right]^2, 100\,\mathrm{mm}\right\}, \qquad \text{(A4)}$$

where zz is also in millimeters and $Bin_{Hi}(i)$ is the upper radius limit of the ith bin. $DOF0 = 2.4054$ is related to the depth of field of the laser array. Equation (A4) gives $zz(1) = 0.594$ mm, $zz(2) = 2.375$ mm, $zz(3) = 5.344$ mm, …, $zz(12) = 85.51$ mm, $zz(13) = 100$ mm. And for all higher bins, zz is also 100 mm.

The final dimension for calculating the volume V in (A2) is related to the flow of air through the laser array. This is just $\overline{U}_{\perp} \Delta t$, where $\overline{U}_{\perp}$ is the average wind speed perpendicular to the laser array during the 30-minute sampling (or sometimes shorter) period (Δt) as measured by the Gill sonic anemometer attached to the cloud imaging probe. I made no corrections for the sonic's being 48 cm above the laser array.

Putting this last result together with (A3) and (A4) in (A2), I finish the algorithm for computing the spray droplet concentration in bin i:

$$C(i) = \frac{10^6 \, \overline{K}_i}{L_{CIP}(i) \; zz(i) \, \overline{U}_{\perp} \; \Delta t \; \Delta r} . \tag{A5}$$

Because L_{CIP} and zz are both expressed in millimeters, we must multiply the right side of (A5) by 10^6 to obtain $C(i)$ in m^{-3} μm^{-1}.

REFERENCES

Andreas, E. L, 1992: Sea spray and the turbulent air-sea heat fluxes. *J. Geophys. Res.*, **97,** 11429–11441.

____, 2002a: Parameterizing scalar transfer over snow and ice: A review. *J. Hydrometeor.*, **3,** 417–432.

____, 2002b: A review of the sea spray generation function for the open ocean. *Atmosphere-Ocean Interactions*, Vol. 1, W. Perrie, Ed., WIT Press, 1–46.

____, 2005: Approximation formulas for the microphysical properties of saline droplets. *Atmos. Res.*, **75,** 323–345.

____, and S. Wang, 2007: Predicting significant wave height off the northeast coast of the United States. *Ocean Eng.*, **34,** 1328–1335.

____, J. B. Edson, E. C. Monahan, M. P. Rouault, and S. D. Smith, 1995: The spray contribution to net evaporation from the sea: A review of recent progress. *Bound.-Layer Meteor.*, **72,** 3–52.

____, K. F. Jones, and C. W. Fairall, 2010: Production velocity of sea spray droplets. *J. Geophys. Res.*, **115,** C12065, doi:10.1029/2010JC006458.

____, L. Mahrt, and D. Vickers, 2012: A new drag relation for aerodynamically rough flow over the ocean. *J. Atmos. Sci.*, **69,** 2520–2537.

____, ____, and ____, 2015: An improved bulk air-sea surface flux algorithm, including spray-mediated transfer. *Quart. J. Roy. Meteor. Soc.*, **141,** 642–654.

Anonymous, 2009: Data analysis user's guide. Chapter II: Single particle imaging. DOC-0223, Rev A, Droplet Measurement Technologies, Inc., Boulder, CO, 34 pp.

____, 2012: Cloud imaging probe (CIP). Manual DOC-0028, Rev L, Droplet Measurement Technologies, Inc., Boulder, CO, 66 pp.

Asplin, M. G., R. Galley, D. G. Barber, and S. Prinsenberg, 2012: Fracture of summer perennial sea ice by ocean swell as a result of Arctic storms. *J. Geophys. Res.*, **117,** C06025, doi:10.1029/2011JC007221.

Brocchini, M., and D. H. Peregrine, 2002: The dynamics of strong turbulence at free surfaces. Part 1. Description. *Advances in Coastal and Ocean Engineering, Vol. 8: Interaction of Strong Turbulence with Free Surfaces*, M. Brocchini and D. H. Peregrine, Eds., World Scientific, 1–41.

Cipriano, R. J., E. C. Monahan, P. A. Bowyer, and D. K. Woolf, 1987: Marine condensation nucleus generation inferred from whitecap simulation tank results. *J. Geophys. Res.*, **92,** 6569–6576.

Clarke, A. D., S. R. Owens, and J. Zhou, 2006: An ultrafine sea-salt flux from breaking waves: Implications for cloud condensation nuclei in the remote marine atmosphere. *J. Geophys. Res.*, **111,** D06202, doi:10.1029/2005JD006565.

de Leeuw, G., F. P. Neele, M. Hill, M. H. Smith, and E. Vignati, 2000: Production of sea spray aerosol in the surf zone. *J. Geophys. Res.*, **105,** 29397–29409.

____, E. L Andreas, M. D. Anguelova, C. W. Fairall, E. R. Lewis, C. O'Dowd, M. Schulz, and S. E. Schwartz, 2011: Production flux of sea spray aerosol. *Rev. Geophys.*, **49,** RG2001, doi:10.1029/2010RG000349.

Fairall, C. W., and S. E. Larsen, 1984: Dry deposition, surface production and dynamics of aerosols in the marine boundary layer. *Atmos. Environ.*, **18,** 69–77.

____, J. D. Kepert, and G. J. Holland, 1994: The effect of sea spray on surface energy transports over the ocean. *Global Atmos. Ocean Syst.*, **2,** 121–142.

____, M. L. Banner, W. L. Peirson, W. Asher, and R. P. Morison, 2009: Investigation of the physical scaling of sea spray spume droplet production. *J. Geophys. Res.*, **114,** C10001, doi:10.1029/2008JC004918.

Gerwick, B. C., Jr., 2007: *Construction of Marine and Offshore Structures*. CRC Press, 813 pp.

Hoppel, W. A., P. F. Caffrey, and G. M. Frick, 2005: Particle deposition on water: Surface source versus upwind source. *J. Geophys. Res.*, **110,** D10206, doi:10.1029/2004JD005148.

Horst, T. W., and J. C. Weil, 1992: Footprint estimation for scalar flux measurements in the atmospheric surface layer. *Bound.-Layer Meteor.*, **59,** 279–296.

____, and ____, 1994: How far is far enough?: The fetch requirements for micrometeorological measurement of surface fluxes. *J. Atmos. Oceanic Technol.*, **11,** 1018–1025.

Hsieh, C.-I, G. Katul, and T.-W. Chi, 2000: An approximate analytical model for footprint estimation of scalar fluxes in thermally stratified atmospheric flows. *Adv. Water Resour.*, **23,** 765–772.

Itagaki, K., 1984: Icing rate on stationary structures under marine conditions. CRREL Rep. 84-12, U.S. Army Cold Regions Research and Engineering Laboratory, 9 pp.

Jones, K. F., and E. L Andreas, 2009: Sea spray icing of drilling and production platforms. ERDC/CRREL Tech. Rep. TR-09-3, U.S. Army Cold Regions Research and Engineering Laboratory, 54 pp.

____, and ____, 2012: Sea spray concentrations and the icing of fixed offshore structures. *Quart. J. Roy. Meteor. Soc.*, **138,** 131–144.

Kaimal, J. C., and J. J. Finnigan, 1994: *Atmospheric Boundary Layer Flows: Their Structure and Measurement*. Oxford University Press, 289 pp.

Kepert, J., C. Fairall, and J.-W. Bao, 1999: Modelling the interaction between the atmospheric boundary layer and evaporating sea spray droplets. *Air-Sea Exchange: Physics, Chemistry and Dynamics*, G. L. Geernaert, Ed., Kluwer, 363–409.

Kljun, N., P. Calanca, M. W. Rotach, and H. P. Schmid, 2004: A simple parameterisation for flux footprint predictions. *Bound.-Layer Meteor.*, **112,** 503–523.

Lewis, E. R., and S. E. Schwartz, 2004: *Sea Salt Aerosol Production: Mechanisms, Methods, Measurements, and Models—A Critical Review*. American Geophysical Union, 413 pp.

Miller, M. A., and C. W. Fairall, 1988: A new parameterization of spray droplet production by oceanic whitecaps. Preprints, *Seventh Conf. on Ocean-Atmosphere Interaction*, Anaheim, CA, Amer. Meteor. Soc., 174–177.

Minsk, L. D., 1984a: Ice observation program on the semisubmersible drilling vessel *SEDCO 708*. CRREL Special Rep. 84-2, U.S. Army Cold Regions Research and Engineering Laboratory, 14 pp.

____, 1984b: Assessment of ice accretion on offshore structures. CRREL Special Rep. 84-4, U.S. Army Cold Regions Research and Engineering Laboratory, 12 pp.

Monahan, E. C., and M. Lu, 1990: Acoustically relevant bubble assemblages and their dependence on meteorological parameters. *IEEE J. Oceanic Eng.*, **15,** 340–349.

____, and I. O'Muircheartaigh, 1980: Optimal power-law description of oceanic whitecap coverage dependence on wind speed. *J. Phys. Oceanogr.*, **10,** 2094–2099.

____, C. W. Fairall, K. L. Davidson, and P. J. Boyle, 1983: Observed inter-relations between 10 m winds, ocean whitecaps and marine aerosols. *Quart. J. Roy. Meteor. Soc.*, **109,** 379–392.

____, D. E. Spiel, and K. L. Davidson, 1986: A model of marine aerosol generation via whitecaps and wave disruption. *Oceanic Whitecaps and Their Role in Air-Sea Exchange Processes*, E. C. Monahan and G. Mac Niocaill, Eds., D. Reidel, 167–174.

Moore, D. J., and B. J. Mason, 1954: The concentration, size distribution and production rate of large salt nuclei over the oceans. *Quart. J. Roy. Meteor. Soc.*, **80,** 583–590.

Muzik, I., and A. Kirby, 1992: Spray overtopping rates for Tarsiut Island: Model and field study results. *Can. J. Civ. Eng.*, **19,** 469–477

Nauman, J. W., 1984: Superstructure icing observations on the semisubmersible *Ocean Bounty* in lower Cook Inlet, Alaska. Proc., *Second International Workshop on Atmospheric Icing of Structures*, Trondheim, Norway, 71–79.

Panofsky, H. A., and J. A. Dutton, 1984: *Atmospheric Turbulence: Models and Methods for Engineering Applications*. John Wiley and Sons, 397 pp.

Peregrine, D. H., 1983: Breaking waves on beaches. *Annu. Rev. Fluid Mech.*, **15,** 149–178.

Perrie, W., and Coauthors, 2012: Selected topics in Arctic atmosphere and climate. *Climatic Change*, **115,** 35–58.

Piazzola, J., G. Tedeschi, and A. Demoisson, 2015: A model for the transport of sea-spray aerosols in the coastal zone. *Bound.-Layer Meteor.*, **155,** 329–350.

Rouault, M. P., P. G. Mestayer, and R. Schiestel, 1991: A model of evaporating spray droplet dispersion. *J. Geophys. Res.*, **96,** 7181–7200.

Smith, M. H., and N. M. Harrison, 1998: The sea spray generation function. *J. Aerosol Sci.*, **29,** Suppl. 1, S189–S190.

____, P. M. Park, and I. E. Consterdine, 1993: Marine aerosol concentrations and estimated fluxes over the sea. *Quart. J. Roy. Meteor. Soc.*, **119,** 809–824.

Soloviev, A., A. Fujimura, and S. Matt, 2012: Air-sea interface in hurricane conditions. *J. Geophys. Res.*, **117,** C00J34, doi:10.1029/2011JC007760.

van Eijk, A. M. J., J. T. Kusmierczyk-Michulec, M. J. Francius, G. Tedeschi, J. Piazolla, D. L. Merritt, and J. D. Fontana, 2011: Sea-spray aerosol particles generated in the surf zone. *J. Geophys. Res.*, **116,** D19210, doi:10.1029/2011JD015602.

Vignati, E., G. de Leeuw, and R. Berkowicz, 2001: Modeling coastal aerosol transport and effects of surf-produced aerosols on processes in the marine atmospheric boundary layer. *J. Geophys. Res.*, **106,** 20225–20338.

Wilson, J. D., 2015: Computing the flux footprint. *Bound.-Layer Meteor.*, **156,** 1–13.

Woolf, D. K., P. A. Bowyer, and E. C. Monahan, 1987: Discriminating between the film drops and jet drops produced by a simulated whitecap. *J. Geophys. Res.*, **92,** 5142–5150.

Wu, J., 1979: Oceanic whitecaps and sea state. *J. Phys. Oceanogr.*, **9,** 1064–1068.

CAPTIONS OF FIGURES

FIG. 1. Mt. Desert Rock. The light gray shading is the island at high tide; the dark gray, the island at low tide. The range between high and low tide is about 3 m. Orange objects are permanent structures: The oval is the lighthouse; the big square is the lightkeeper's house. The red circle on the small square is the cloud imaging probe and associated sonic anemometer/thermometer mounted on the foghorn platform. The three-legged symbol denotes the "turbulence tripod." The quadrant 260° to 7° indicates the only wind directions I retained for my analyses. The arcs at 50 and 75 m show that all samples collected by the cloud imaging probe were within 75 m of the water; and, at high tide, most were much closer.

FIG. 2. The cloud imaging probe from Droplet Measurement Technologies and the Gill sonic anemometer/thermometer mounted on the foghorn platform on Mt. Desert Rock.

FIG. 3. Wind speed, air temperature, and relative humidity during the experiment on Mt. Desert Rock (MDR). All legends refer to all panels. "MDR NOAA" identifies the NOAA instruments on the lighthouse; likewise, "Matinicus" denotes the NOAA instruments on Matinicus Rock. "Gill Sonic on MDR" is wind speed from the Gill sonic anemometer associated with the cloud imaging probe. "Our Data" identifies the wind speed and temperature data from the turbulence tripod.

FIG. 4. Surface water temperature and salinity and significant wave height ($H_{1/3}$) during the experiment on Mt. Desert Rock. In the temperature and salinity panels, the data identified as "Ours" are from manual bucket samples. In the wave height panel, our estimate of $H_{1/3}$ comes from the Andreas and Wang (2007) algorithm and the wind speed from the Gill sonic anemometer.

FIG. 5. Near-surface spray droplet concentration spectra (i.e., C_0 from (3.5)) for wind speeds (U_{N10}) between 6 and 10 m s^{-1}. The black and red curves distinguish between measurements made during high water and low water, respectively. The green curve is the fit to these concentration spectra, (4.5), where the U_{N10} used to calculate each green curve is the middle value of the indicated wind speed range.

FIG. 6. As in Fig. 5 but for wind speeds between 10 and 17 m s^{-1}.

FIG. 7. All the concentration spectra (e.g., Figs. 5 and 6) measured in wind speeds (U_{N10}) of 5 m s^{-1} and higher are nondimensionalized with the respective concentration measured in the radius bin centered at 6.25 μm. Hence, all spectra are identically one for r_0 = 6.25 μm. The plot still distinguishes measurements made during high water from those made during low water. The plot also shows the bin medians for all the data and, individually, for the high-water and low-water data. The small-radius bins and the large-radius bins fall along straight lines in this log-log plot (the two black lines). I thus represent the median nondimensional spectrum with a hyperbola, (4.3) with a = 0.10.

FIG. 8. All concentration data in the 333 runs are normalized and plotted against U_{N10}. The normalization is for each radius bin such that all concentrations measured in that bin are divided by the bin average. The data are identified as to whether they were collected during high water or low water. Three fitting lines are shown: one calculated using least-squares linear regression as y-versus-x, one taken as the bisector of y-versus-x and x-versus-y fits, and one for which a U_{N10}^3 dependence is assumed.

FIG. 9. The near-surface spray concentration data (i.e., C_0) for the bin centered at r_0 = 6.25 μm are plotted versus the neutral-stability wind speed at 10 m, U_{N10}. The blue line is the best-fitting cubic relation through these data, (4.4).

FIG. 10. The Mt. Desert Rock (MDR) spray generation function, (5.1), as a number flux for various values of the wind speed at a reference height of 10 m, U_{10}. For these calculations, the surface temperature (T_s) was 1°C; the air temperature (T_r), 0°C; the relative humidity (RH_r), 80%; the surface salinity, 34 psu; and the barometric pressure, 1000 mb. For comparison, the plot also shows the joint Monahan et al. (1986) and Fairall et al. (1994) function (from Andreas et al. 2010).

FIG. 11. The ratio of surf-zone production to open-ocean production of spray, as predicted by (6.5), is plotted as a function of 10-m wind speed (U_{10}) for the γ values indicated. As explained in the text, in (6.5) F = 200 m, R = 30 m, S comes from (6.1), and $W(U_{10})$ comes from (5.4).

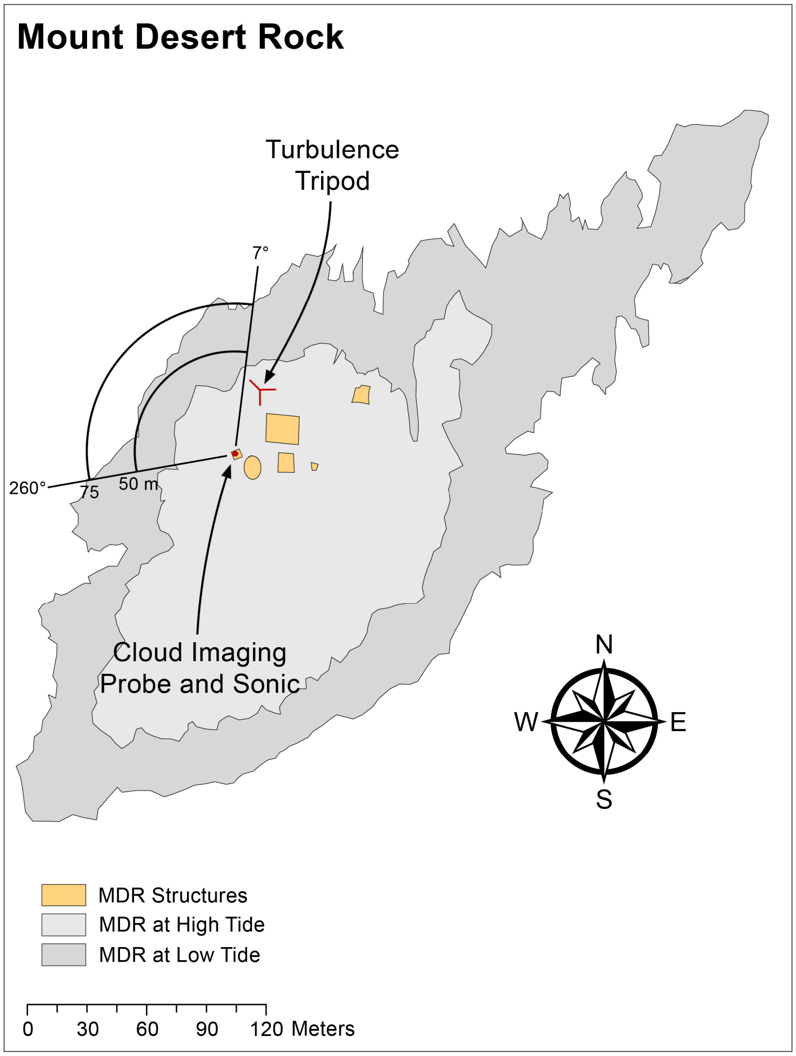

FIG. 1. Mt. Desert Rock. The light gray shading is the island at high tide; the dark gray, the island at low tide. The range between high and low tide is about 3 m. Orange objects are permanent structures: The oval is the lighthouse; the big square is the lightkeeper's house. The red circle on the small square is the cloud imaging probe and associated sonic anemometer/thermometer mounted on the foghorn platform. The three-legged symbol denotes the "turbulence tripod." The quadrant 260° to 7° indicates the only wind directions I retained for my analyses. The arcs at 50 and 75 m show that all samples collected by the cloud imaging probe were within 75 m of the water; and, at high tide, most were much closer.

FIG. 2. The cloud imaging probe from Droplet Measurement Technologies and the Gill sonic anemometer/thermometer mounted on the foghorn platform on Mt. Desert Rock.

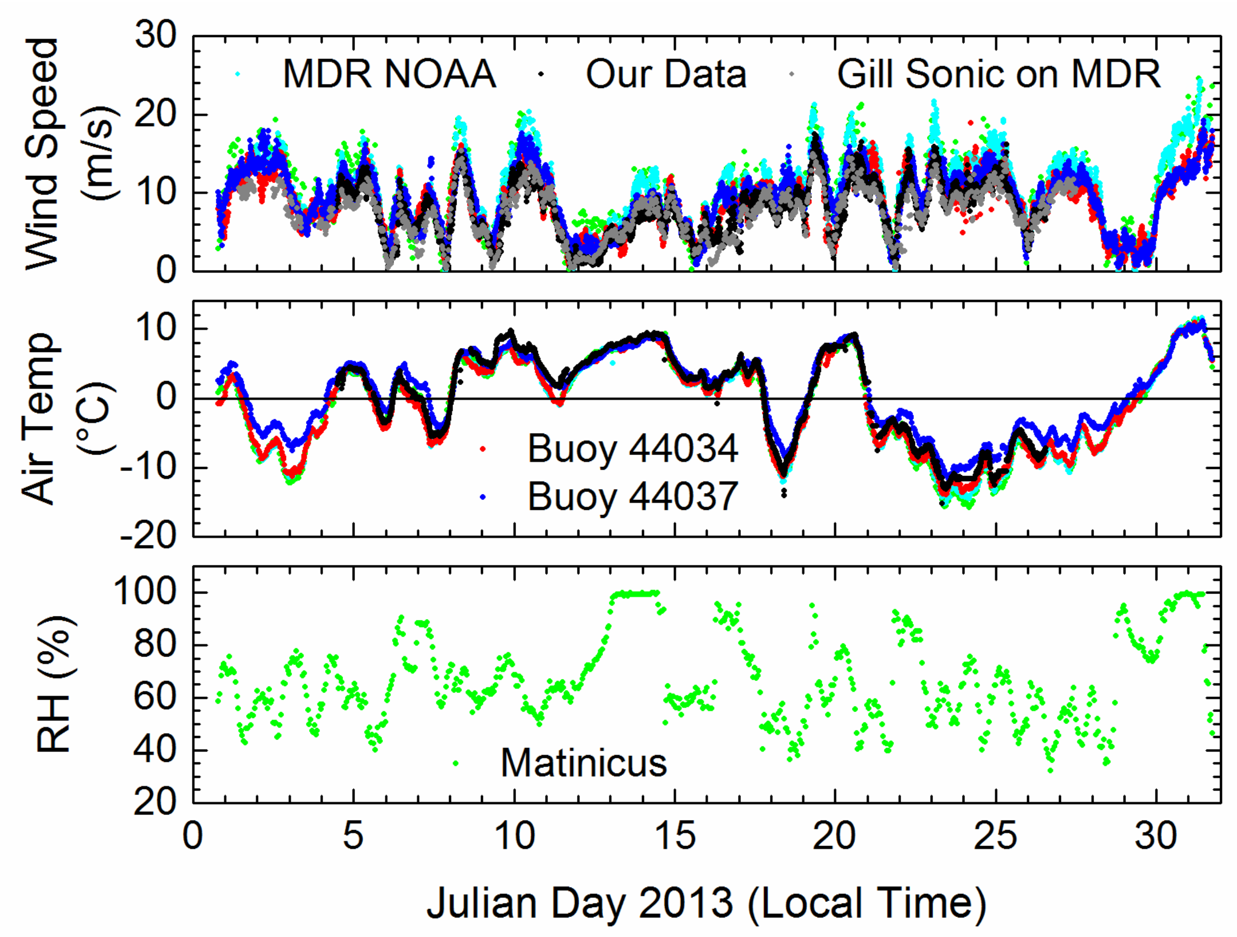

FIG. 3. Wind speed, air temperature, and relative humidity during the experiment on Mt. Desert Rock (MDR). All legends refer to all panels. “MDR NOAA” identifies the NOAA instruments on the lighthouse; likewise, “Matinicus” denotes the NOAA instruments on Matinicus Rock. “Gill Sonic on MDR” is wind speed from the Gill sonic anemometer associated with the cloud imaging probe. “Our Data” identifies the wind speed and temperature data from the turbulence tripod.

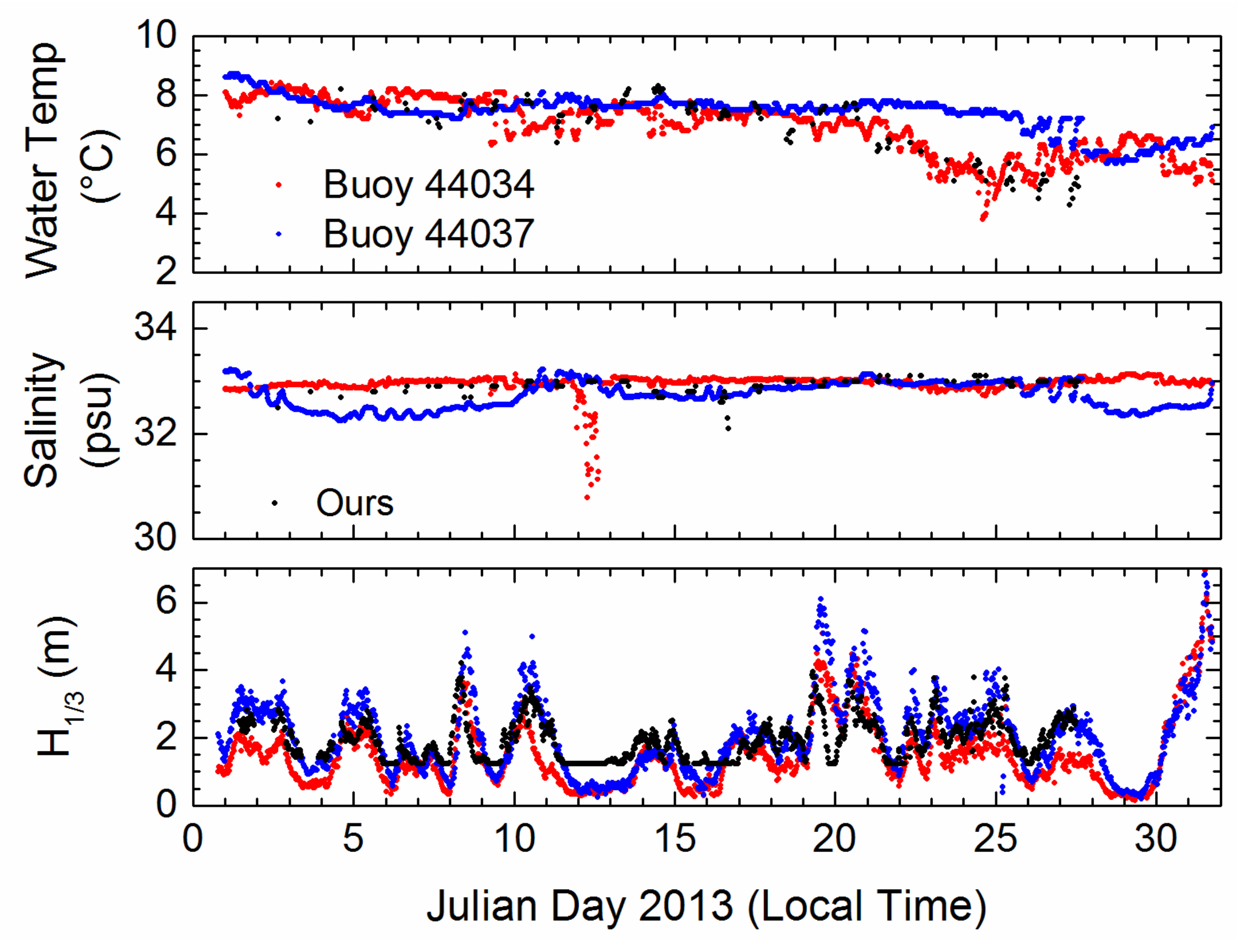

FIG. 4. Surface water temperature and salinity and significant wave height ($H_{1/3}$) during the experiment on Mt. Desert Rock. In the temperature and salinity panels, the data identified as "Ours" are from manual bucket samples. In the wave height panel, our estimate of $H_{1/3}$ comes from the Andreas and Wang (2007) algorithm and the wind speed from the Gill sonic anemometer.

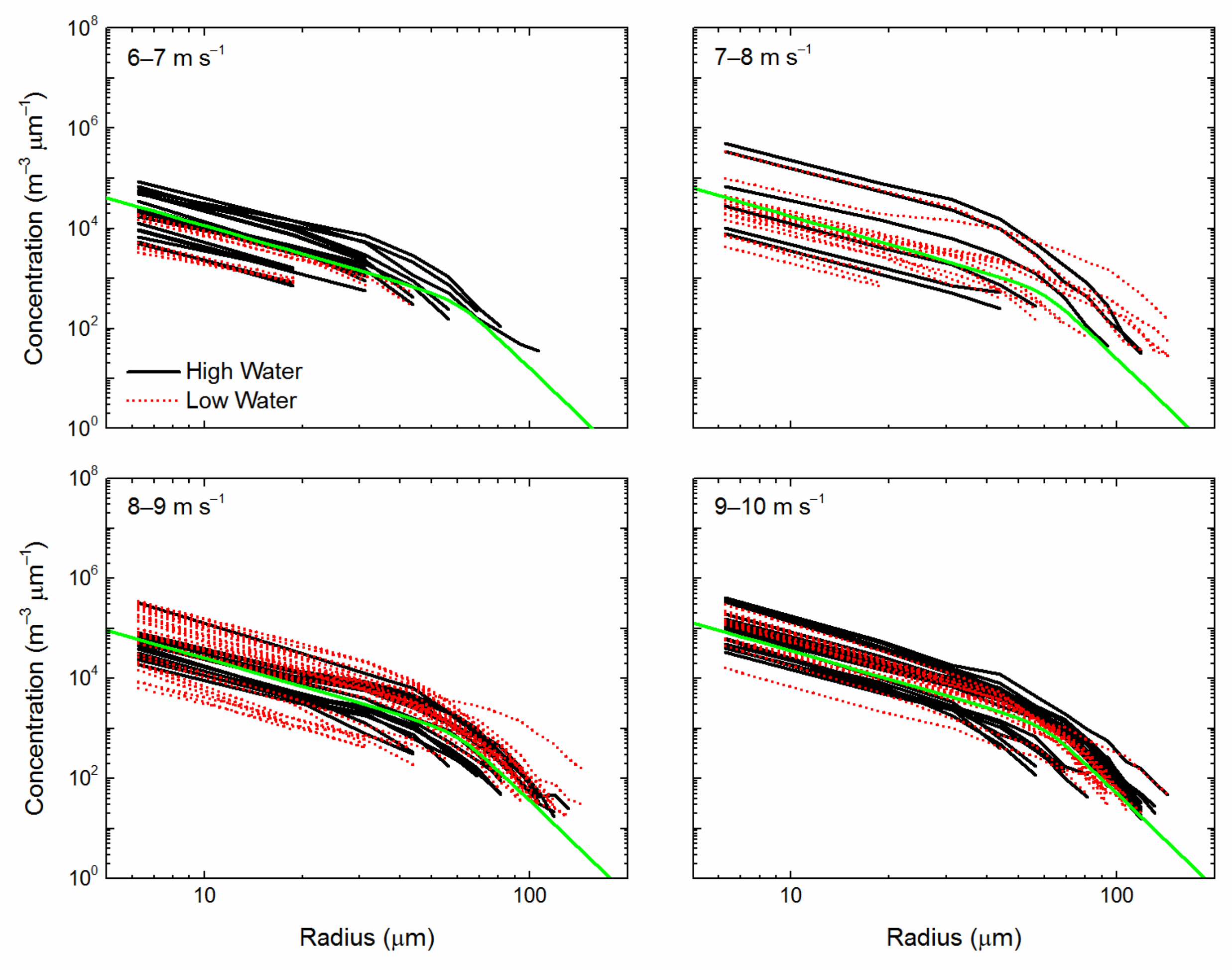

FIG. 5. Near-surface spray droplet concentration spectra (i.e., C_0 from (3.5)) for wind speeds (U_{N10}) between 6 and 10 m s^{-1}. The black and red curves distinguish between measurements made during high water and low water, respectively. The green curve is the fit to these concentration spectra, (4.5), where the U_{N10} used to calculate each green curve is the middle value of the indicated wind speed range.

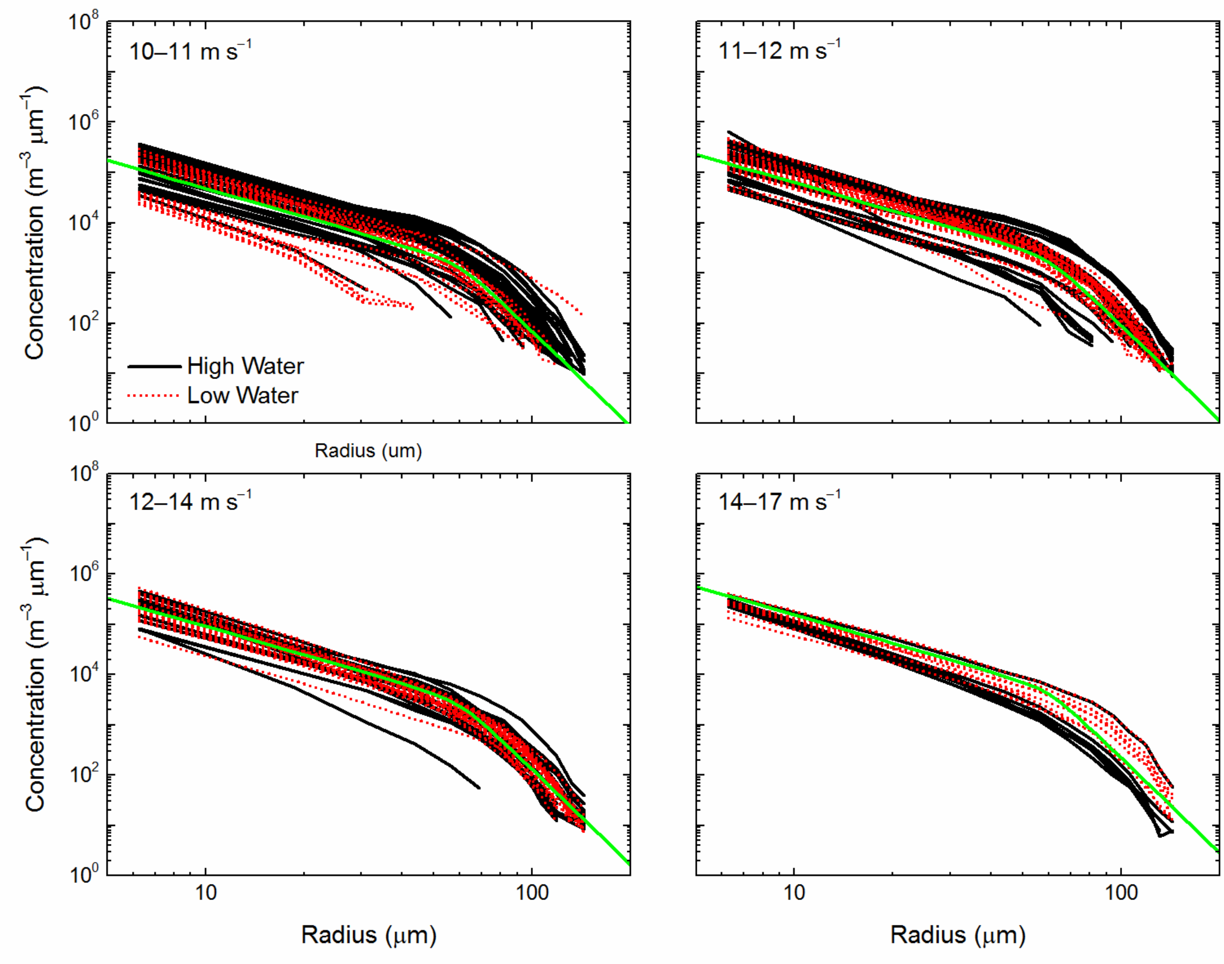

FIG. 6. As in Fig. 5 but for wind speeds between 10 and 17 m s^{-1}.

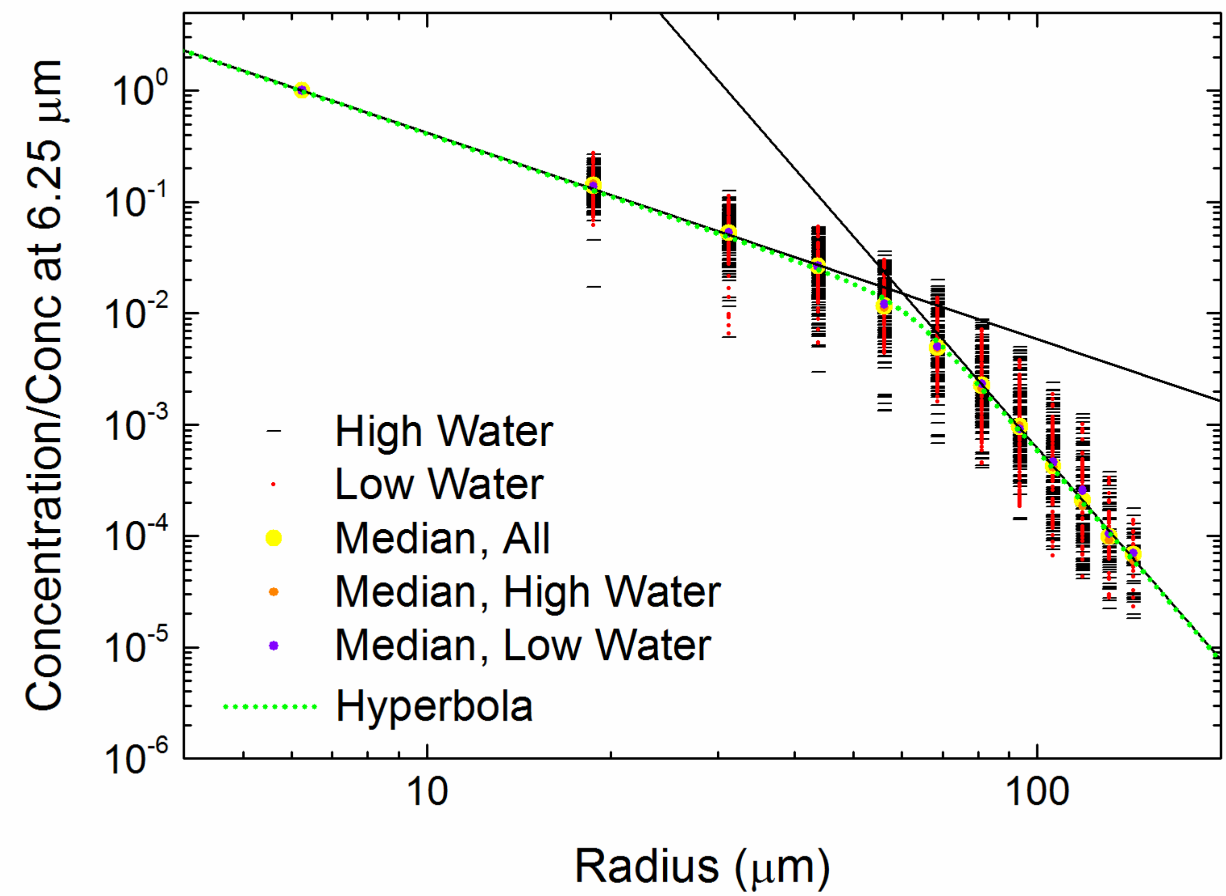

FIG. 7. All the concentration spectra (e.g., Figs. 5 and 6) measured in wind speeds (U_{N10}) of 5 m s^{-1} and higher are nondimensionalized with the respective concentration measured in the radius bin centered at 6.25 μm. Hence, all spectra are identically one for r_0 = 6.25 μm. The plot still distinguishes measurements made during high water from those made during low water. The plot also shows the bin medians for all the data and, individually, for the high-water and low-water data. The small-radius bins and the large-radius bins fall along straight lines in this log-log plot (the two black lines). I thus represent the median nondimensional spectrum with a hyperbola, (4.3) with a = 0.10.

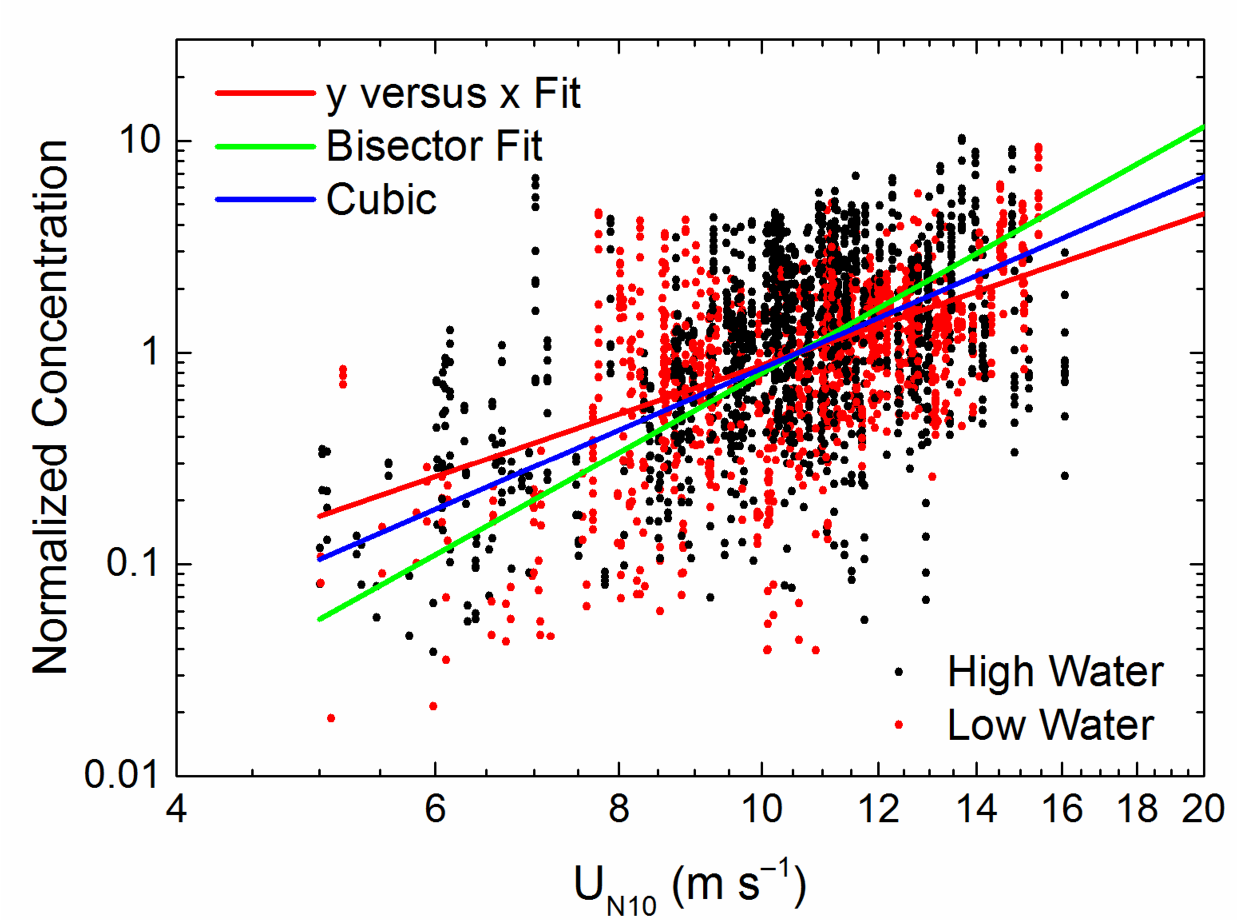

FIG. 8. All concentration data in the 333 runs are normalized and plotted against U_{N10}. The normalization is for each radius bin such that all concentrations measured in that bin are divided by the bin average. The data are identified as to whether they were collected during high water or low water. Three fitting lines are shown: one calculated using least-squares linear regression as *y*-versus-*x*, one taken as the bisector of *y*-versus-*x* and *x*-versus-*y* fits, and one for which a U_{N10}^{3} dependence is assumed.

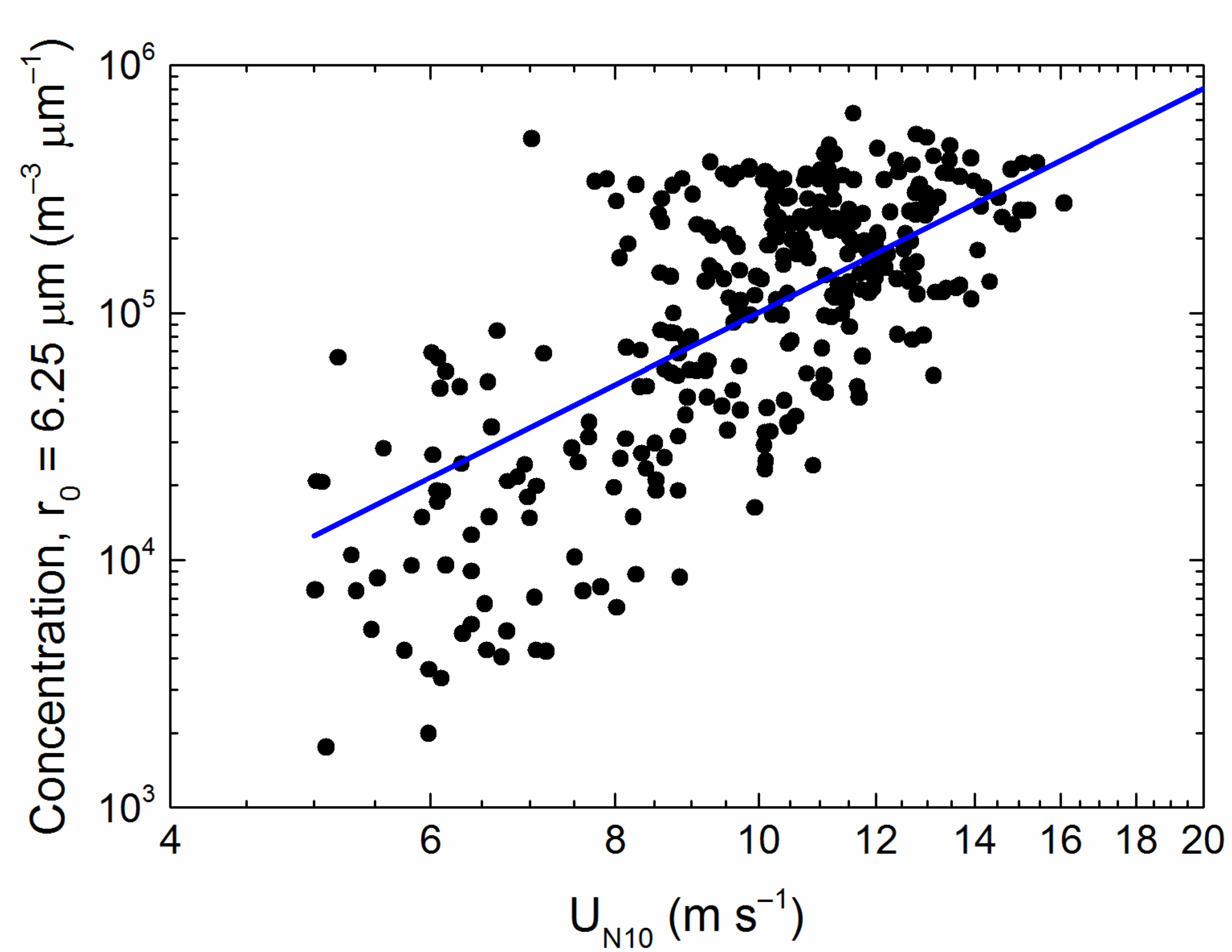

FIG. 9. The near-surface spray concentration data (i.e., C_0) for the bin centered at r_0 = 6.25 µm are plotted versus the neutral-stability wind speed at 10 m, U_{N10}. The blue line is the best-fitting cubic relation through these data, (4.4).

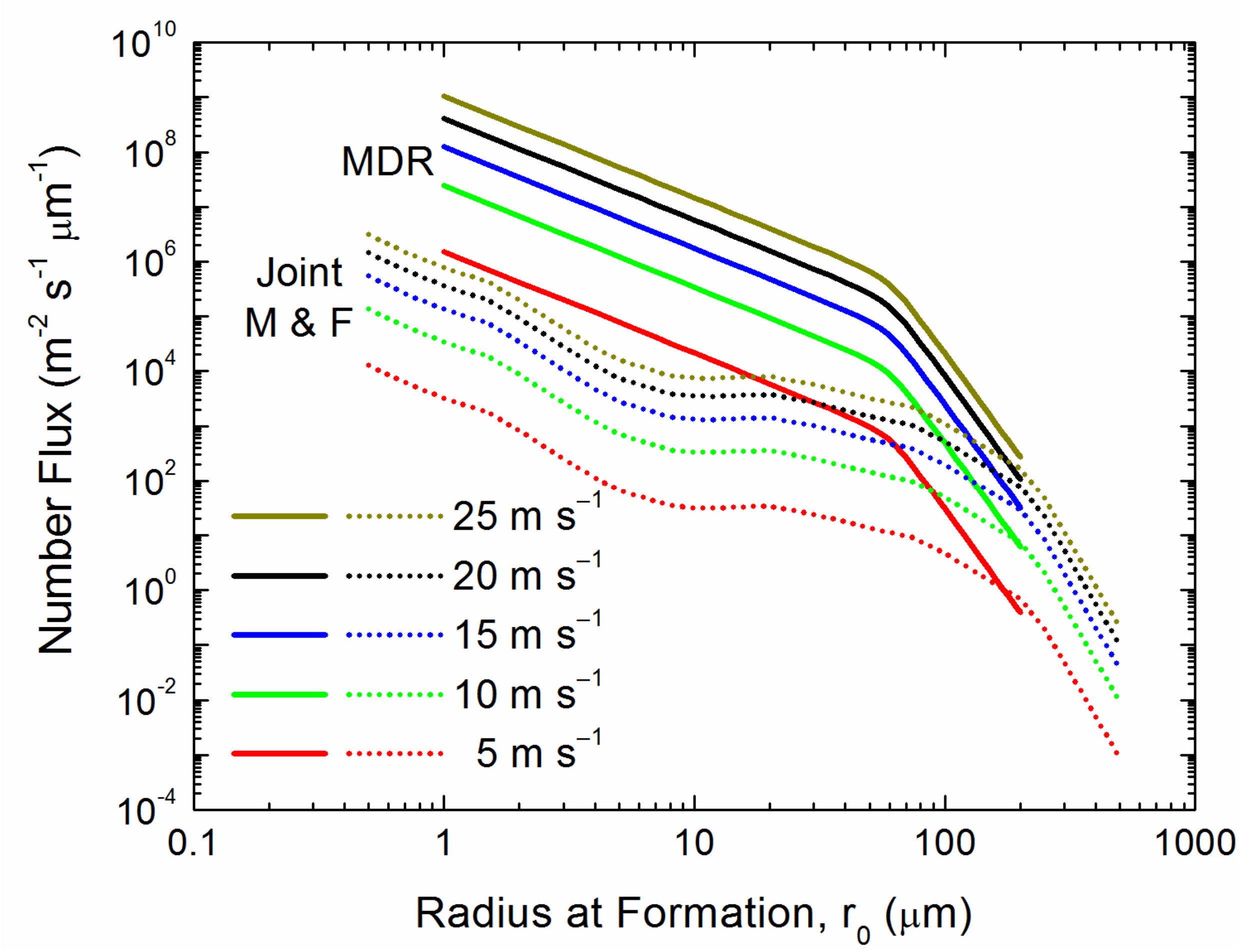

FIG. 10. The Mt. Desert Rock (MDR) spray generation function, (5.1), as a number flux for various values of the wind speed at a reference height of 10 m, U_{10}. For these calculations, the surface temperature (T_s) was 1°C; the air temperature (T_r), 0°C; the relative humidity (RH_r), 80%; the surface salinity, 34 psu; and the barometric pressure, 1000 mb. For comparison, the plot also shows the joint Monahan et al. (1986) and Fairall et al. (1994) function (from Andreas et al. 2010).

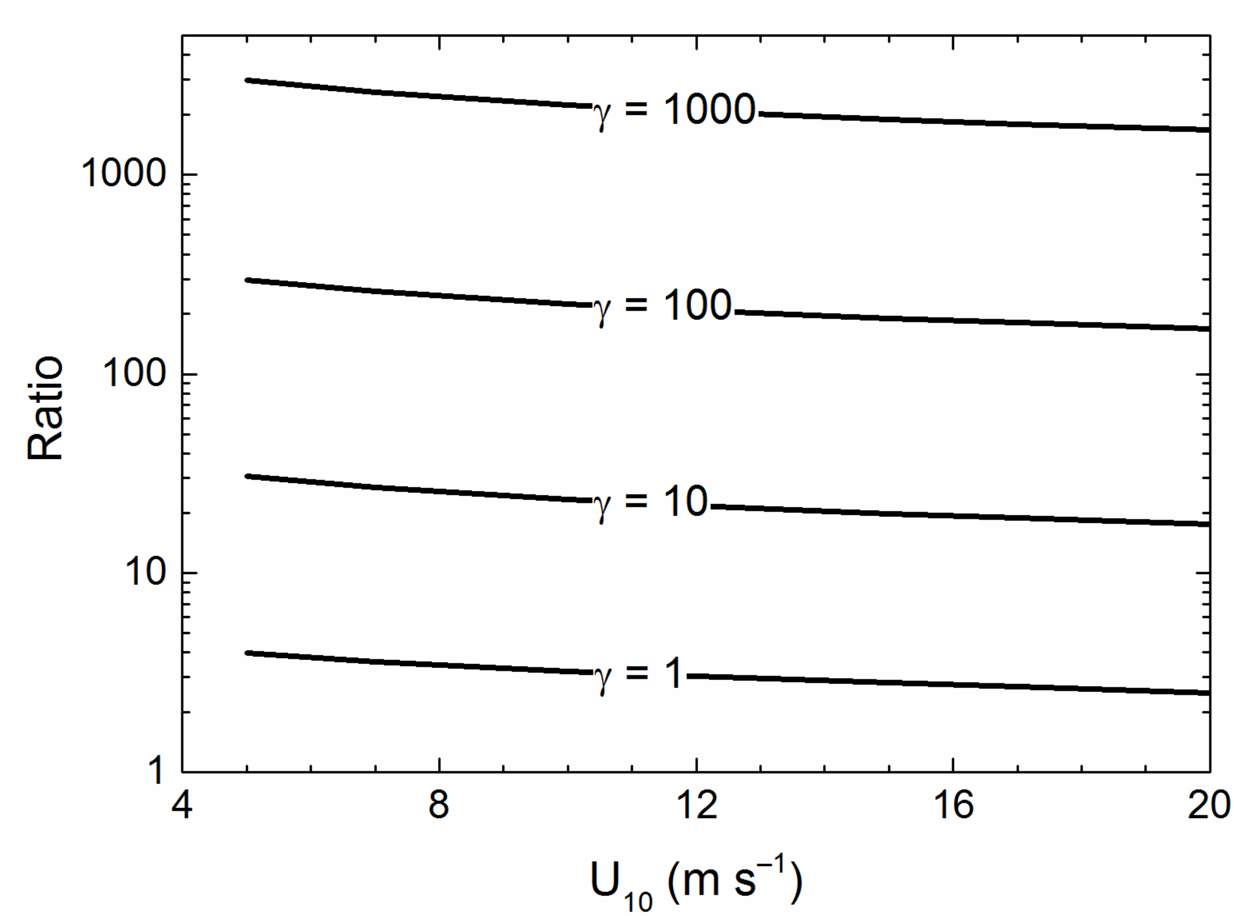

FIG. 11. The ratio of surf-zone production to open-ocean production of spray, as predicted by (6.5), is plotted as a function of 10-m wind speed (U_{10}) for the γ values indicated. As explained in the text, in (6.5) F = 200 m, R = 30 m, S comes from (6.1), and $W(U_{10})$ comes from (5.4).